Imaging As-Grown Interstitial Iron Concentration on Boron-Doped Silicon Bricks via Spectral Photoluminescence

Bernhard Mitchell, Daniel Macdonald, Jonas Schön, Jürgen W. Weber, Hannes Wagner, and Thorsten Trupke

Abstract—The interstitial iron concentration measured directly on the side face of a silicon brick after crystallization and brick squaring can give important early and fast feedback regarding its material quality. Interstitial iron is an important defect in crystalline silicon, particularly in directionally solidified ingots. Spectral photoluminescence intensity ratio imaging has recently been demonstrated to independently provide high-resolution bulk lifetime images and is therefore ideally suited to assess spatially variable multicrystalline silicon bricks. Here, we demonstrate this technique to enable imaging of the interstitial iron concentration on boron-doped silicon bricks and thick silicon slabs. We present iron concentration studies for two directionally solidified silicon bricks of which one is a standard multicrystalline and the other is a seeded-growth ingot. This lifetime-based measurement technique is highly sensitive to interstitial iron with detection limits down to concentrations of about 1×10^{10} cm^{-3}. Its accuracy is enhanced, as the injection level remains below 2×10^{12} cm^{-3} during the measurement and, hence, avoids the influence of injection level dependences on the conversion factor, although it remains dependent on the knowledge of the electron capture cross section of interstitial iron in silicon. Access to both bulk lifetime and dissolved iron concentration provides a valuable parameter set of as-grown crystal quality and the relative recombination fraction of interstitial iron via Shockley–Read–Hall (SRH) analysis. Simulated interstitial iron concentration profiles support the presented experimental data.

Index Terms—Bricks, dissolved iron, imaging, ingot, interstitial iron, photoluminescence (PL), silicon.

B. Mitchell is with the Australian Centre for Advanced Photovoltaics and the School of Photovoltaic and Renewable Energy Engineering, University of New South Wales, Kensington, N.S.W. 2052, Australia (e-mail: bernhard.mitchell@unsw.edu.au).

D. Macdonald is with the Research School of Engineering, The Australian National University, Canberra, A.C.T. 2601, Australia (e-mail: daniel.macdonald@anu.edu.au).

J. Schön is with the Fraunhofer Institute for Solar Energy Systems, 79110 Freiburg, Germany (e-mail: jonas.schoen@ise.fraunhofer.de).

J. W. Weber is with BT Imaging Pty Ltd., Waterloo, N.S.W. 2017, Australia (e-mail: j.weber@btimaging.com).

H. Wagner is with the Department of Solar Energy, Leibniz University of Hanover, 30167 Hannover, Germany (e-mail: wagner@solar.uni-hannover.de).

T. Trupke is with the Australian Centre for Advanced Photovoltaics and the School of Photovoltaic and Renewable Energy Engineering, University of New South Wales, Kensington, N.S.W. 2052, Australia, and also with BT Imaging Pty Ltd., Waterloo, N.S.W. 2017, Australia (e-mail: t.trupke@unsw.edu.au).

I. INTRODUCTION

INTERSTITIAL iron contamination plays a major role in silicon photovoltaics, especially if the bulk absorber is p-doped silicon [1], [2]. Its role in directionally solidified material is not primarily due to the contamination of the polysilicon feedstock, since the remaining iron is mostly segregated to the top of the ingot. Instead, iron is introduced mostly from the crucible material (SiO_2) and crucible linings (Si_3N_4) during directional solidification [3]–[5]. With its mid-band gap defect level, interstitial iron can limit the cell performance of p-base solar cells after standard, extended, or even high-temperature gettering steps [6]–[8]. The properties of interstitial iron, which include its solubility, diffusivity, [9], and precipitation [10], [11], have been studied and modeled extensively [12]–[16] in multicrystalline silicon (mc-Si).

Various measurement techniques for the study of interstitial iron in silicon ingot have been developed. In the past, height profiles were usually measured via the analysis of a series of wafers [17], [18]. Only recently different approaches measuring lifetimes directly on the brick surface had been demonstrated. Two of them are based on the sensing of the photoconductance (PC) signal [19]–[21], while two others are based on photoluminescence (PL) techniques [22], [23]. Only PC measurements have been used for interstitial iron concentration measurements on brick level so far [20], [21].

The interstitial iron concentration is often referred to as the "dissolved" iron concentration, since no substitutional iron has been found in a nondistorted, i.e., implanted or irradiated crystal configuration [9]. Even small concentrations of interstitial iron atoms have an impact on the silicon material's lifetime, allowing for concentrations down to $\sim 1 \times 10^{10}$ cm^{-3} to be detected through lifetime-based analyses [3], [24], [25]. In addition, the time-dependent Fe–B dissociation signal has been used on wafers for the measurement of the interstitial iron concentration [26]. Interestingly, the total iron concentration can be orders of magnitude higher [3], [12], [18] than the interstitial concentration due to a large fraction of precipitated iron and is assessable most sensitively via neutron activation analysis or various mass spectroscopy measurements including GDMS, SIMS, or ICPMS [17], [18], [27]. Interstitial iron is highly mobile in the silicon lattice at elevated temperatures during diffusion and firing [9], [28]. Therefore, understanding the precipitation, dissolution, and gettering behavior of iron is of major importance for successful defect engineering during cell processing [10], [11], [29].
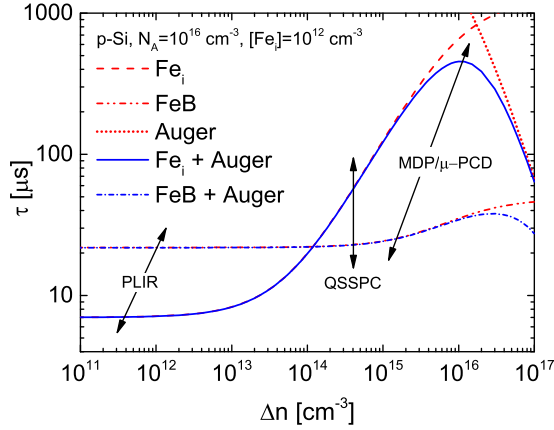
Fig. 1. Expected carrier lifetimes due to Fe_i and Fe–B pairs in boron-doped silicon with $N_A = 10^{16}$ cm^{-3} and an iron concentration of 10^{12} cm^{-3} as a function of the excess carrier density Δn. Auger recombination and its impact on the lifetimes at high injection are also shown. The typical injection regions in which PLIR, QSSPC, and MDP/μ-PCD operate are indicated and appear angled if utilizing a constant generation rate.

This paper extends the use of PL imaging from the measurement of the interstitial iron concentration on passivated silicon wafers [25], [30] to measuring directly on the unpassivated brick surface. We demonstrate the measurement of bulk lifetimes on unpassivated surfaces before and after iron–boron (Fe–B) pair dissociation using the spectral photoluminescence intensity ratio (PLIR) analysis [31], [32]. Experimental work is performed on directionally solidified boron–doped silicon bricks, as it is the most widely used type of ingot crystallization in the photovoltaic industry [33].

In this paper, we also report on the advancement of the PL-based analysis of silicon bricks in low-signal areas, such as the bottom of the brick, allowing this section of the brick to be included in the quantitative analysis. Note that prior to this work, preliminary data were included in [34].

II. THEORY AND METHODS

The measurement of the interstitial iron concentration presented in this study is based on the technique first introduced by Zoth and Bergholz [35]. The technique has been demonstrated to be a sensitive measure of the dissolved iron concentration on boron-doped surface-passivated silicon wafers [30], [35]. It is based on the pairing reaction that interstitial iron undergoes with the acceptor boron after the exposure to illumination of sufficient intensity to dissociate the initial equilibrium paired iron boron state [36]. The dissociation of iron–boron pairs reflects on the minority carrier bulk lifetime due to their different defect levels (see Fig. 1). Hence, the interstitial iron concentration can be derived by

$$[Fe_i] = C(\Delta n, N) \left\{ \frac{1}{\tau_{b,f}} - \frac{1}{\tau_{b,i}} \right\} \quad (1)$$

where $\tau_{b,i}$ and $\tau_{b,f}$ are the initial and the final bulk lifetime, i.e., before and after Fe–B pair breaking. The conversion factor C depends on the injection level, the doping concentration, as

well as the energy levels and captures cross sections of the Fe_i and Fe–B states [37]. A generalized formulation can be found in [30].

For a defined sample preparation, care needs to be taken to only dissociate the iron–boron pairs and not to also activate boron–oxygen (BO) complexes during pair breaking [24]. For this purpose, short and intensive flash illuminations are ideal. Importantly, by using the described approach, we assume that other defect channels affecting the recombination lifetime are not altered during the pair-breaking process and cancel out when subtracted

$$\frac{1}{\tau_{b(f,i)}} = \frac{1}{\tau_{(FeB,Fe_i),SRH}} + \frac{1}{\tau_{b,Auger}} + \frac{1}{\tau_{b,Other}}. \quad (2)$$

The spectral PLIR analysis permits to take bulk lifetime images at true low-injection conditions, which simplifies the analysis of the C-factor as it becomes independent of the injection level below about 2×10^{12} cm^{-3}. Fig. 1 depicts the injection-level-dependent carrier lifetime considering a single defect level of either Fe_i or Fe–B in boron-doped silicon. PC-based techniques that have been used to measure dissolved iron on silicon bricks operate above the crossover point, largely because PC measurements show experimental artefacts related to minority carrier trapping at medium to low injections. The surface photovoltage technique is also able to measure at true low-injection conditions but has yet to be demonstrated on silicon bricks to our knowledge [38]. As a result of measuring under medium-to high-injection conditions, PC techniques are forced to analyze C for every data point individually and might also need to account for Auger effects, as shown in Fig. 1.

Low-injection measurement conditions ensure that minimal Fe–B pair splitting occurs during the measurements themselves and minimize the impact from nonuniform injection levels into the depth of the sample [39]. An additional benefit is that the impact of the doping variation of typically $0.8 - 2 \times 10^{16}$ cm^{-3} on the C-factor can be neglected in this measurement regime [37]. In our Shockley–Read–Hall (SRH) modeling throughout this paper, we use the capture cross sections and energy levels from [40], but chose $\sigma_n^{Fe_i} = 1.3 \times 10^{-14}$ cm^2 from [30].

Lifetime measurements shown in this study are performed on the bare brick surface without surface passivation. However, a surface polish prior to the measurement eliminates effects resulting from variations in the surface roughness. The measurement on polished bricks allows for 1-D modeling of the transfer function.

III. EXPERIMENT

A. Dissociation

The C-factor of (1) is dependent on the ratio of the concentrations of dissolved Fe present as Fe–B or Fe_i after dissociation. Ideally, all Fe–B pairs should be dissociated for a maximum lifetime signal. Partial dissociation is difficult to quantify and, hence, is a source of uncertainty.

We used a Broncolor flash lamp, which provides up to 3200 J per flash with a time constant of 2 ms and a 5500K equivalent Xenon discharge spectrum at a distance of 5 cm to

the sample. Since the bulk lifetime analysis used in this study is based on the analysis of two PL images taken with different spectral filters, we applied a continuous series of 80 flashes before taking the first long-pass filtered image of the dissociated state. We then applied another 20 flashes directly before the second short-pass filtered image to minimize the impact of repairing. Both PL images were taken with a short exposure of 5 s. We minimized the time between the end of the flash series and the start of each PL measurements to less than 10 s.

We calculate a Fe–B association time constant $\tau_{\mathrm{assoc}} = 2093$ s for a boron concentration of 1×10^{16} cm^{-3} [41]. Hence, after a maximum delay of 15 s, i.e., from the application of the flash light to the end of the measurement, we estimate that less than 1% of the dissociated Fe–B pairs will reform [42]. Therefore, we can neglect this effect for the samples investigated in this study. However, the repairing fraction can become significant for higher acceptor concentrations typically found in metallurgically purified and compensated silicon.

We estimate the dissociation fraction by assuming that a minimum of 1000 suns (100 W/cm^2) for a time greater than 1 ms per flash is incident on the sample. In practice, it is difficult to calibrate such an intense flash intensity on a silicon absorber, but we believe this to be a conservative estimate for a 3200-J Xenon flash lamp. Recart et al. achieved about 1000 suns using a similar flash lamp but with only half the energy rating (i.e., 1600 J) [43]. We compute the minority carrier generation depth profiles for a 5500K black body illumination spectrum for various bulk lifetimes using the device simulator PC1D [44]. The dissociation fraction can then be estimated following Geerligs and Macdonald [36], who found that the dissociation rate Γ_d for recombination dominated by Fe–B centers is given by

$$\Gamma_d = K \times \frac{G^2}{[\mathrm{FeB}]^2} \tag{3}$$

with $K \approx 5 \times 10^{-15}$ s, G denoting the minority carrier generation rate, and [FeB] the concentration of Fe–B pairs.

Since the concentration of the Fe–B pairs and other defects are not known before the measurement, we can, at this point of the analysis, only assume that Fe–B is the dominant defect and associate carrier lifetimes to Fe–B concentrations through an SRH calculation. We correlate a carrier lifetime of 1 μs to a Fe–B concentration of $\sim 2.2 \times 10^{13}$ cm^{-3}, 10 μs to $\sim 2.2 \times 10^{12}$ cm^{-3}, and 100 μs to $\sim 2.2 \times 10^{11}$ cm^{-3}. In practice, other recombination channels might reduce the actual Fe–B dissociation rate and an iterative approach feeding the measured dissolved iron concentration back into the denominator of (3) could improve the analysis. The proportionality factor K reduces in the presence of other recombination channels, but generalized quantitative analyses are not available in the literature [36].

We further simplify the analysis by not accounting for the injection dependence of the minority carrier lifetime during dissociation and use $G = \frac{\Delta n}{\tau}$. This is a conservative simplification, since lifetimes in Fe–B or Fe$_i$ dominated material only increase for injection levels exceeding 2×10^{12} cm^{-3}. In addition, we
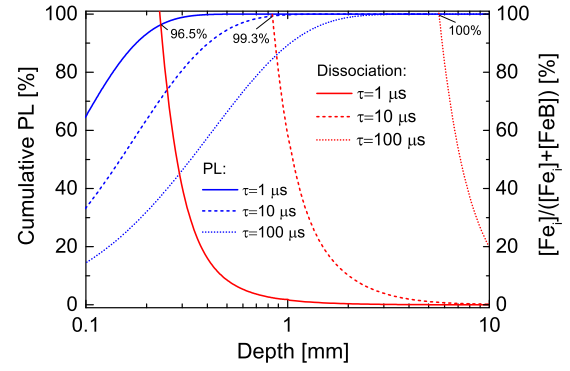

Fig. 2.   Evaluation of the dissociation fraction for 1, 10, and 100 μs of minority carrier bulk lifetime for dominating recombination through Fe–B defect and $K = 5 \times 10^{-15}$ s. A xenon flash intensity of 1000 suns and a series of more than 50 flashes, each with a peak duration of 1 ms, ensure almost complete dissociation of the bulk from which PL is collected for most relevant lifetimes. Shallow injection at bulk lifetimes below 1 μs results in partial dissociation but still ensures dissociation of 90% or above and with only minor impact on the analysis of the interstitial iron concentration.

assume the bulk lifetime being constant throughout the application of the flash light onto the brick's surface. However, in reality, the fraction of interstitial iron increases with the number of flashes applied depending on the depth and local lifetime. We find this to also be a conservative simplification, since we obtain injection levels above the crossover point during dissociation at 1000-sun illumination in regions of the bulk that contribute to the detected PL. Hence, the local bulk lifetimes will increase throughout the series of flashes applied leading to higher dissociation rates in reality than calculated in this assessment.

With the above assumptions, we calculate a dissociation depth profile as a function of bulk lifetime and determine the dissociation fraction by evaluating the relative cumulative PL at 100% dissociation (see Fig. 2), i.e., we determine the fraction of the measured PL signal, which originates from the fully dissociated region. The cumulative PL represents the long-pass filtered signal here.

Using conservative estimates of a 1000-sun flash intensity and a series of 50 flashes, we calculate complete dissociation for most of the lifetime range with only lifetimes below about 5 μs resulting in fractions below 99%. In case Fe–B is not the dominating defect, the recombination through the Fe–B defect is reduced and a lower dissociation rate is expected. Note that a precise analysis is not possible to date, since there are no published data for K available that would describe these other cases. However, it is clear that if bulk lifetimes are below 10 μs and Fe–B is not dominating the recombination, a higher than 1000-sun flash intensity would need to be used. In typical directionally solidified silicon material, low lifetimes usually correlate with Fe–B being the dominant defect. This indicates that full dissociation is likely achieved for typical brick faces using the above approach. Care would need to be taken if high-purity crucibles and linings are used as Fe–B may not be the major recombination path in the highly contaminated parts of the ingot [3], [4].
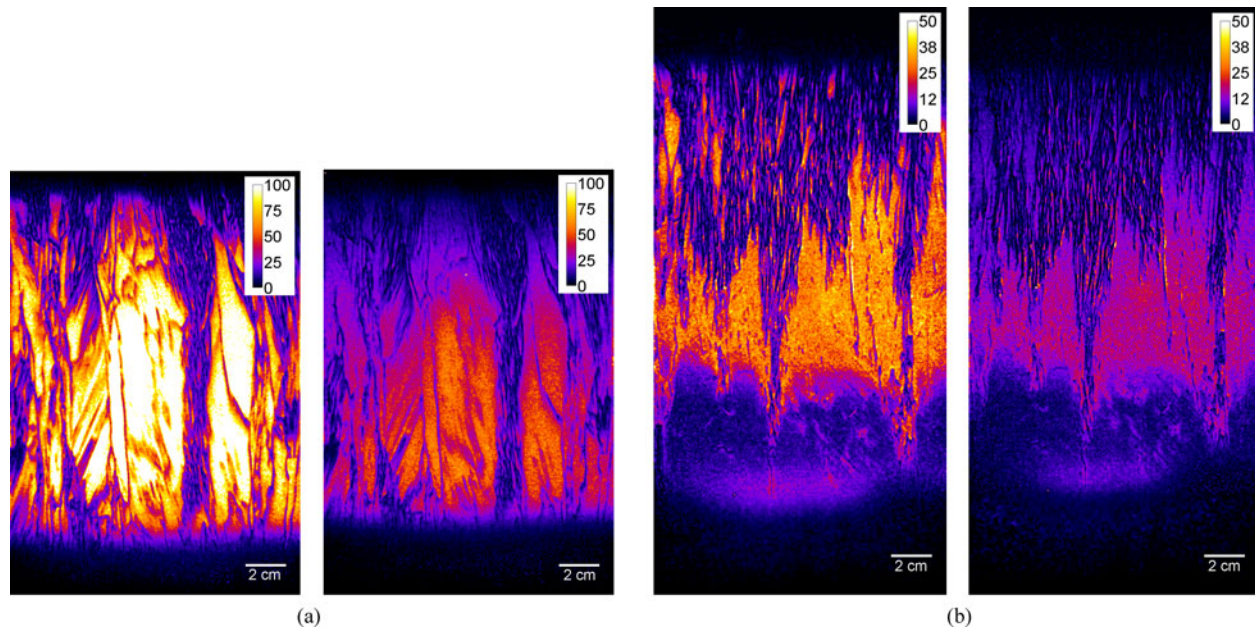
Fig. 3.   Spectral PLIR detected bulk lifetime images before and after complete Fe–B pair dissociation for (a) standard- and (b) seeded-growth silicon brick. As-grown bulk lifetimes are given in μs at weighted average injection levels ranging from 1×10^{11} to 1×10^{12} cm^{-3}.

B. Spectral Photoluminescence Intensity Ratio and Bulk Lifetimes

Highly resolved bulk lifetime images were analyzed before and after pair dissociation employing the spectral PLIR analysis on both the standard and the seeded-growth brick (see Fig. 3). The spectral PLIR method has been described previously in [31] and [32]. It utilizes the bulk lifetime-dependent shift in spectral PL emission to quantify the silicon minority carrier bulk lifetime. Two full-field images are taken with different spectral filtering to maximize the difference in PL emission throughout the relevant bulk lifetimes and are then rated through an intensity ratio to bulk lifetime transfer function. The transfer function is derived using a 1-D model incorporating analytical models for the excess-carrier density profile and the spectral PL emission. The technique has been found to provide absolute bulk lifetime images of directionally solidified and Cz-grown silicon bricks without the need for a separate background doping scan. However, it can only provide a lower than 20% relative uncertainty on bulk lifetime, if spreading of light in the detection device can be either prohibited or compensated for. The light spreading was found to significantly deteriorate the analysis [32]. Hence, using either an appropriate direct semiconductor detector (e.g., In–Ga–As) or applying a deconvolution process is critical. Moreover, the 1-D model does not accurately describe the regions that incorporate lattice imperfections, such as grain boundaries or dislocations. Thus, these limited areas cannot be quantified accurately using spectral PLIR and will also result in localized artefacts in the interstitial iron concentration imaging (see Fig. 4) [45].

Note that for a fast industrial application of the interstitial iron concentration scan, it is desirable to measure the lifetime of the paired state prior to the application of the flash and the
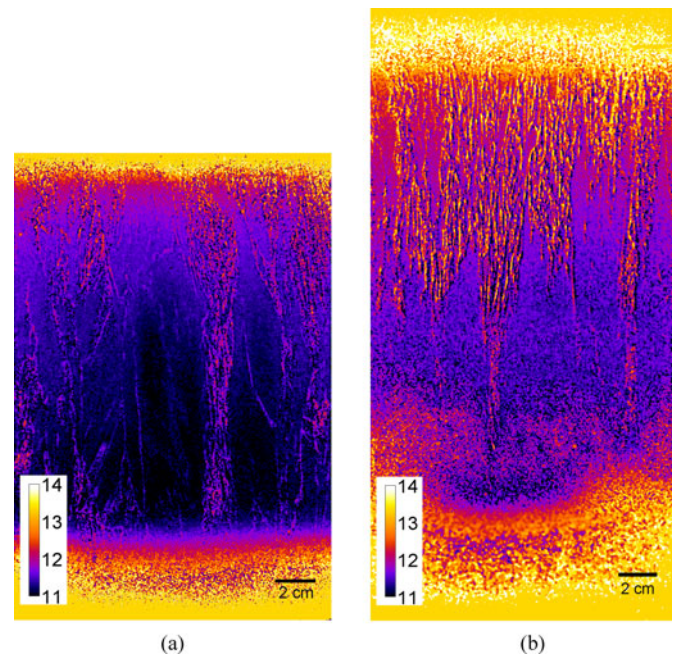

Fig. 4.   Log$_{10}$ [Fe$_i$] images of (a) standard- and (b) seeded-growth mc-Si bricks. As-grown dissolved iron concentrations are given in cm^{-3}. The highly contaminated top and bottom sections of the brick cannot be measured in full field and are colored with reference to Fig. 8.

measurement of the lifetime of the dissociated state and avoid any waiting period. However, in samples of higher oxygen concentration and/or boron concentration, some BO complexes may be activated through the application of an intense flash light and possibly impact the lifetime [46]. The uncertainty for these types
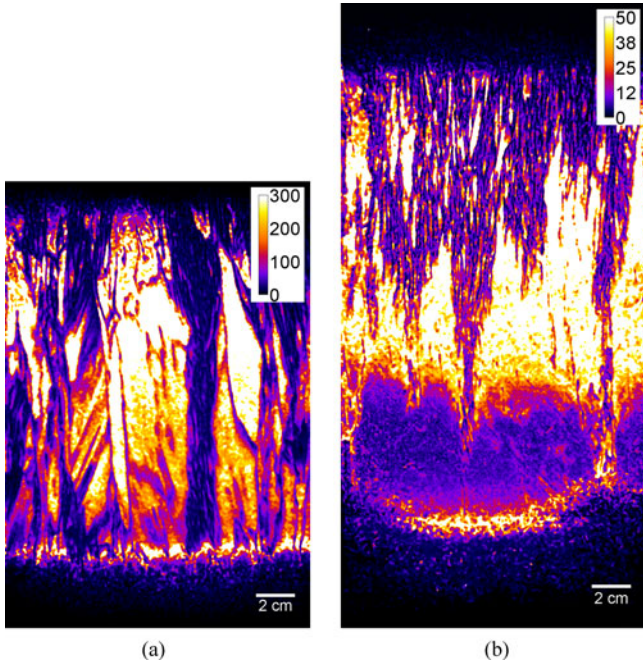
Fig. 5. $\tau_{b,\mathrm{other}}$ images of (a) standard- and (b) seeded-growth Si bricks depicting the as-grown bulk lifetime due to defects other than dissolved iron. The images are calculated from Figs. 3 and 4 using the SRH defect recombination model. Bulk lifetimes are given in μs for injection levels ranging from 1×10^{11} to 1×10^{12} cm^{-3}. The standard-growth brick has a lower concentration of other defects within the grains after iron removal than the seeded-growth brick. The seeded-growth brick shows a higher defect distribution in the lower central part of the brick.

of samples can easily be eliminated if the lifetime of the dissociated state is measured first and if a sufficient amount of time is given for a full repair [47] of the iron–boron pairs to occur prior to the measurement of the lifetime of the paired and possible partially activated state.

Imaging the interstitial iron concentration using the spectral PLIR method is particularly challenging, since the signal-to-noise ratio (SNR) is reduced by the low-injection requirements of the interstitial iron imaging. Reduced laser intensity and short exposure are vital for the elimination of the influence of significant dissociation or repairing during the measurement. We take images at 0.1-sun equivalent (0.01 W/cm^2) illumination intensity and an exposure time of 5 s. The main reason to measure with such low laser intensity is to ensure true low-injection conditions, which simplifies the C-factor analysis (see Fig. 1) [37]. We calculate weighted average injection levels [48] of 4.4×10^{11} cm^{-3} to 1.2×10^{12} cm^{-3} for 1- and 200-μs bulk lifetime, respectively. The dissociation of iron–boron pairs during the measurement is minimal at these low-injection levels. Calculations are limited to the case of dominant Fe–B defects [36] but indicate the dissociation time constant to remain at least two orders of magnitude longer than the applied 5-s exposure time for any bulk lifetime typically found in boron-doped photovoltaic silicon (DS-mc and Cz). We employ 3×3 pixel binning to improve the SNR. This limits the resolution to about 0.5×0.5 mm^2 per pixel.

Image processing becomes a crucial part of the interstitial iron analysis, since it is extremely sensitive to noise. We apply image deconvolution with regularization to all PL images [49] to reduce the noise intensification throughout the analysis. Fig. 3 shows the direct comparison of the bulk lifetime images before and after Fe–B pair dissociation for both bricks. The standard-growth brick shown in Fig. 3(a) was cropped at the top and bottom section prior to this analysis and, hence, appears with smaller low-lifetime regions at the bottom and the top. The cropping of some of the highly contaminated sections (top, bottom, edge) is a common practice in current manufacturing, as these sections cannot usually be processed into efficient solar cells [50]. The standard-growth brick was grown in a generation 4 (G4) crucible with a total height prior to cropping of 25 cm (see Fig. 9), whereas the seeded-growth ingot, shown in Fig. 3(b), was grown in a G5 crucible and its total (ingot) height is 30 cm. The seeded-growth brick reveals some interesting lifetime features in the bottom region with a large region of lower lifetime, which may be due to some solid state in-diffusion of other point defects. The image also illustrates that extended dislocation networks appear toward the top half of the ingot, which are commonly found in seeded-growth material and remain a obstacle of this growth technique. Overall, the lifetimes of this particular seeded-growth sample are considerably lower before and after pair breaking than in the standard-growth sample.

IV. RESULTS

A. Dissolved Iron Imaging

The determination of the C-factor from (1) is a crucial element of the quantitative imaging analysis of dissolved iron. We find both the injection and the doping dependence of C are negligible in the true low-injection measurement regime used with weighted average injection levels ranging from 1×10^{11} to 1.2×10^{12} cm^{-3} and a doping variation from $0.5 - 1.5 \times 10^{16}$ cm^{-3}. For this range, we calculate $C = 1.06 \times 10^{13}$ μs $\cdot$ cm^{-3}. The C-factor can vary significantly for higher injection levels or doping concentration, as modeled by Macdonald *et al.* [37].

Fig. 4 presents the corresponding iron concentration images for both standard- and seeded-growth silicon bricks and is presented on a logarithmic scale. Our measurements reveal that the lowest interstitial iron concentrations are located in the central region, whereas increased concentrations are found toward the bottom and the top of the brick. This is the typcial profile of a directionally solidified ingot and in accordance with previous wafer and brick-based measurements [21]. Hence, the interstitial iron concentration seems to follow a macroscopically 1-D distribution with height in the standard-growth brick, which is only interrrupted by grain and dislocation structures locally. The seeded-growth brick shows some interesting nonhomogenous iron contamination in the bottom areas, indicating some other defect contamination. Overall, interstitial iron concentrations in the range 9×10^{10} cm^{-3} to above 5×10^{12} cm^{-3} are found. Higher levels of interstitial iron contamination in the central area of the brick are found in the seeded-growth sample at around 3×10^{11} cm^{-3}.
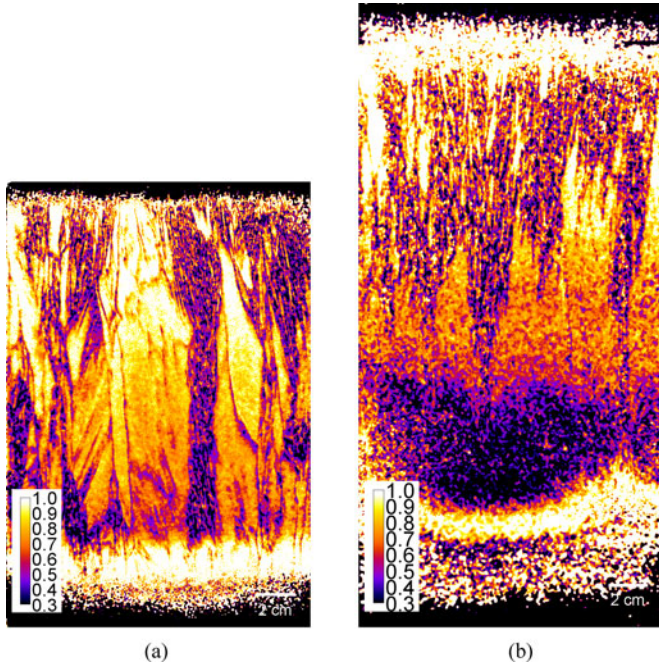
Fig. 6. Images of the relative fraction of dissolved iron related recombination of total recombination for (a) standard mc-Si and (b) seeded-growth Si brick for injection levels ranging from 1×10^{11} to 1×10^{12} cm^{-3}. No quantitative data could be extracted in the highly contaminated bottom and top sections of the bricks using the full-field measurement. These areas mostly appear in black. The bottom of the standard-growth brick (a) was subsequently measured separately using a masking approach and is found to be 100% dominated by dissolved iron (see Fig. 8).

We note that the spectral PLIR method is limited in resolving small features such as small grains and dislocation clusters quantitatively. These limitations were discussed in previous publications [32], [45]. Artefacts in the bulk lifetime images near such small features affect the measured dissolved iron concentration near grain boundaries, which often appears to be higher than in nearby grains. Wafer studies and simulations have found that in the as-grown state, the interstitial iron concentration is higher within the grain, which switches after phosphorous gettering [10], [25]. The highly contaminated bottom and top areas of the brick cannot be resolved quantitatively using the full-field spectral PLIR analysis. We will discuss this limitation and introduce an alternative quantitative approach for these areas.

B. Imaging Residual Recombination Lifetime Without Fe

Access to both bulk lifetime and dissolved iron concentration allow the calculation of the contribution of the dissolved iron to the bulk lifetime and thus permit quantifying the residual impact of other recombination centers that influence the recombination lifetime in case the dissolved iron is removed. We can derive the bulk lifetime after iron removal with reference to (2):

$$\tau_{b,\text{other}} = \left[\frac{1}{\tau_{b,f}} - \frac{1}{\tau_{\text{SRH,Fe}_i}} \right]^{-1} \tag{4}$$

where $\tau_{b,\text{other}}$ is the recombination bulk lifetime due to recombination centers other than interstitial iron, and $\tau_{\text{SRH,Fe}_i}$ is the

SRH lifetime for the interstitial iron defect of the measured concentration in the silicon lattice.

In the past, $\tau_{b,\text{other}}$ was interpreted as a "potential lifetime" obtained after the effective gettering of interstitial iron [51], [52]. A predictive value is expected if effective gettering can reduce the interstitial iron to concentrations that no longer impact on the effective lifetime of the final cell.

Recent studies have shown that iron silicide precipitates can be partially dissolved into the silicon crystal during the high-temperature phosphorous diffusion process [10], [11], [53] and even during the final firing of the contacts [7]. In addition, the reverse process of internal precipitation from the interstitial site can be introduced by thermal anneals [54]. These mechanisms may impact on the predictive value of $\tau_{b,\text{other}}$ in practice.

Images of $\tau_{b,\text{other}}$ are depicted for both brick faces in Fig. 5, revealing a relatively stronger influence of the iron contamination on the bulk in the standard-growth brick, despite the fact that the standard-growth brick contains a lower total dissolved iron concentration. Bulk lifetimes of up to 300 μs are predicted for this brick if all interstitial iron is removed. The seeded-growth brick would also achieve significantly higher lifetimes after interstitial iron removal, but the impact is less significant and the overall bulk lifetime would remain mostly below 50 μs. This indicates the presence of other impurities or structural defects (e.g., oxygen precipitates or interstitials, SiC, iron precipitates). Since the difference in bulk lifetime of the seeded-growth brick is not related to interstitial iron, and unlikely to another interstitial metal impurity, it would probably largely remain after phosphorous gettering and limit the performance of the device.

C. Recombination Fraction Imaging

Knowledge of both bulk lifetime and interstitial iron concentration also allows the calculation of the recombination that is due to interstitial iron as a fraction of the total recombination using the SRH recombination model. The analysis provides another piece of information for as-grown bricks/ingots and reveals that interstitial iron is the dominant recombination path in both the bottom and top low-lifetime sections at the analyzed injection level for both bricks (see also separate analysis of the bottom below). Overall, interstitial iron is a more dominant recombination path in the standard-growth brick than in the seeded-growth brick (see Fig. 6). And this is even though the iron point defect contamination in the standard-growth brick is lower. A large region in the lower part of the seeded-growth brick is not dominated by recombination through the interstitial iron defect, indicating the presence of another strong recombination channel in this section of the brick. The region also does not show the typical planar distribution as that expected from normal growth conditions with horizontal solidification planes.

V. Discussion

A. Quantitative Analysis of Low-Lifetime Bottom Section–Extension of Standard Analysis

PL images that are captured during full-field illumination suffer from light spreading effects [49]. In particular, spectral
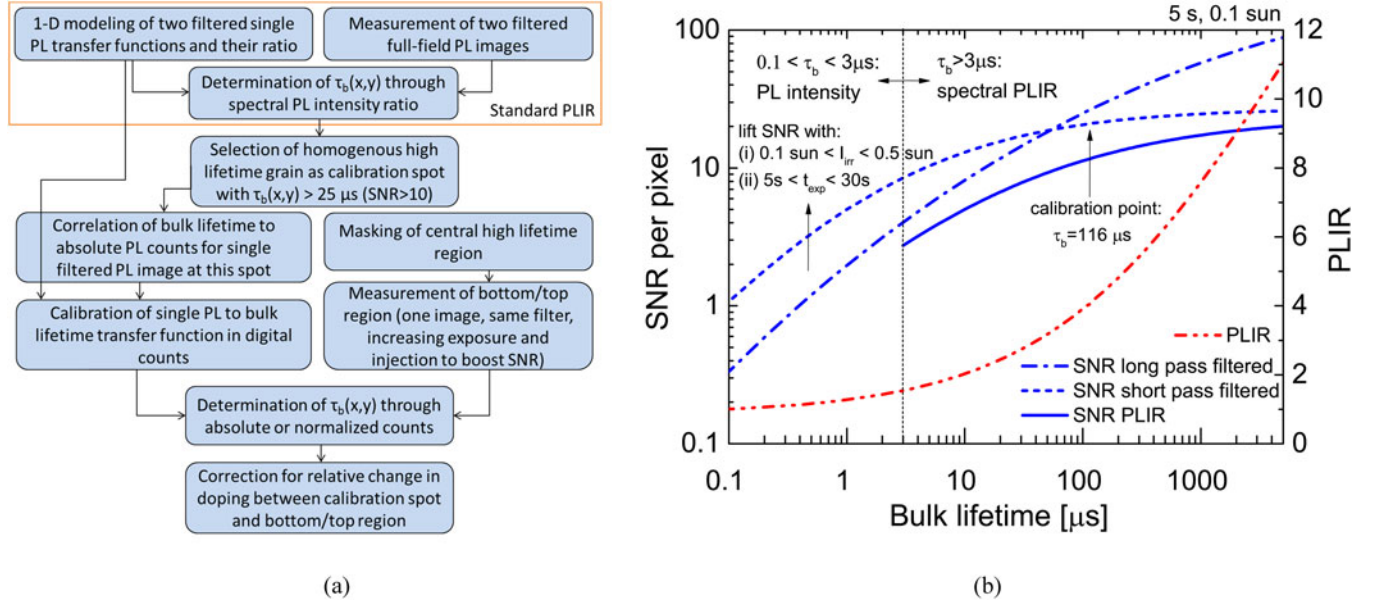
Fig. 7.   (a) Flowchart of the extended spectral PLIR analysis for the analysis of the bottom/top region of brick. (b) SNRs of long- and short-pass filtered signal as a function of bulk lifetime for a typical measurement of dissolved iron (0.1 suns, 5-s exposure, 3×3 binning) and the measurement equipment (CCD camera, lens, filter) used in this study. The SNR functions that are obtained from the theoretical analysis are calibrated at a large central grain of $\tau_b = 116$ μs on the standard-growth brick. The PLIR ratio is shown for comparison indicating a small functional dependence on the bulk lifetime below about 3 μs that in combination with the low SNR is insufficient to determine the bulk lifetime through a direct spectral ratio analysis at 0.1-sun illumination intensity and 5-s exposure time. The low SNR below 3 μs can be improved by increasing the laser intensity and the exposure time within the stated range.

analyses of the PL response are highly sensitive to this if using a Si CCD camera for detecting silicon luminescence [32]. Thus, a deconvolution restoration is crucial for quantitative analyses with methods such as spectral PLIR.

We see a dynamic lifetime and luminescence intensity range of more than two orders of magnitude within a short distance of a few centimeters in the transition region from the contaminated regions (bottom, top, edge) to the higher purity central area on directionally solidified silicon bricks [32]. Although the abrupt intensity drop can be localized and quantified using spectral PLIR after deconvolution restoration, the residual light spreading toward the low-emitting bottom and top section interferes with its quantitative analysis too strongly, even after such restoration.

A simple but effective physical masking of the region of high PL emission in the center of the brick during the measurement can overcome this limitation [32]. If PL is only detected on the low-signal top and bottom regions, the signal variation within one PL image is reduced to a factor of typically ~3, which is down from ~100 (see Fig. 7). The spreading of PL intensity from high-lifetime regions is thereby effectively avoided.

However, we find that a spectral PLIR analysis alone still cannot give quantitative results in the bottom or top section of the brick, even if the dynamic signal range is reduced and light spreading from the central area is negligible. Our theoretical analysis shows that this is due to a diminishing lifetime signal in the spectral PLIR transfer function for lifetimes below about 3 μs (see Fig. 7). Therefore, we propose an extended approach that allows us to calibrate the PL intensity of a measured *single* image to bulk lifetimes.

The method introduced here is based on the spectral PLIR method used above but also utilizes the fact that we have calculated the relative PL intensity to bulk lifetime transfer functions for both short- and long-pass image detection. These relative functions are normally used to determine the PLIR to bulk lifetime transfer function through taking the ratio of the individual transfer functions (see [31] and [32]). Hence, we first measure the brick in full field without any masking and analyze its bulk lifetime using the standard spectral PLIR method. Second, we pick a central high-lifetime large grain for which we have just determined the bulk lifetime using the spectral signal and then identify the measured count rates of the same area on the individual short- and long-pass source images. We thereby establish a PL intensity to bulk lifetime pair for both *single* images. This leaves us with a calibrated count rate for the lifetime of the respectively selected grain. Finally, we know through the calculation the relative single PL to bulk lifetime transfer function. As a result, we are able to calibrate the calculated relative PL to bulk lifetime transfer functions to PL count rates for any bulk lifetime anywhere on the image including the bottom and top sections of the brick, where the detected PL intensity is extremely low. Once we have calibrated the single PL intensity to bulk lifetime transfer function, we mask the central high-lifetime area and measure the bottom and top a second time without changing the illumination intensity. The exposure time is typically increased to 30 s to improve the SNR. Additionally, it is also possible to increase the laser intensity for the measurement of the low-lifetime bottom/top section to up to 0.5 suns. This can be done without reaching the injection-dependent regime (see Fig. 1) or dissociating a significant fraction of the Fe–B pairs. The measured
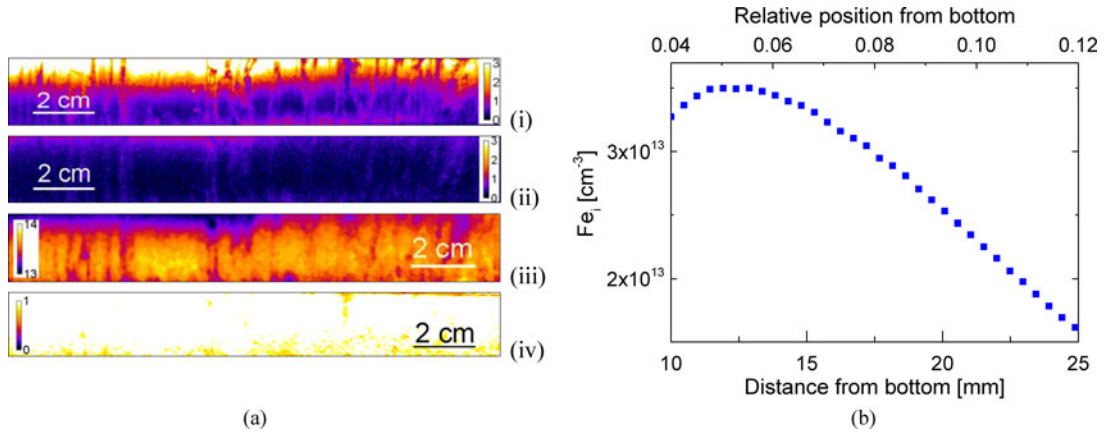
Fig. 8.   (a) Bulk lifetime images of the bottom 2 cm of standard mc-Si brick face. (i) Before and (ii) after Fe–B pair breaking analyzed via spectral PLIR calibrated total PL analysis. The corresponding Log_{10} [Fe_i] and relative recombination fraction are shown in (iii) and (iv). Some laterally inhomogeneous iron is revealed in (a, iii). (b) Cross-sectional averaged dissolved iron concentration as a function of brick height of the same region. Absolute and relative positions in (b) are given relative to the full as-grown ingot prior to any cropping.

PL intensity is proportional to the exposure time; hence, it can easily be normalized. Then, we can derive the bulk lifetimes through the measured absolute or normalized count rates and the single image transfer function. Note that care needs to be taken if the bottom/top is measured with different laser intensity than that central part. A laser intensity calibration is crucial to determine the exact change in photon flux.

Fig. 7 depicts this analysis for the measurement apparatus used in this study and shows that there is only a small spectral ratio signal for bulk lifetimes below about 3 μs for our particular filter combination. Fig. 7 clarifies that the SNR would hardly be sufficient for a quantitative spectral analysis below about 3 μs. However, the total count rates we find are sufficient to quantify bulk lifetimes for either short- or long-pass filtered images. The long-pass filtered signal does not saturate to higher lifetimes, but provides lower SNR at low lifetimes. The selection of the more suitable calibrated transfer function is, hence, a question that needs to be answered that is dependent on the detection systems filtering and the bulk lifetime of the selected calibration point.

Importantly, the calibration of the PL intensity into bulk lifetime is strictly only valid for an area with constant doping, as the doping contributes linearly to the total signal under low injection (PL $\propto \Delta n N$). The variation of the dopant concentration in boron-doped directionally solidified ingots is limited in the bottom half of the brick [55]. Thus, this approach can be applied to the bottom of the brick without introducing significant uncertainty if the calibration spot is located in the bottom half of the brick. The approach can be extended to the top if additional doping measurements are available (e.g., via eddy current) or less accurately if the doping profile is estimated via the Scheil equation [55]. Note that the doping variation in the single PL images does not severely affect the interstitial iron concentration, since its contribution to the PL signal affects both the absolute count rate before and after the iron–boron pair splitting.

From the total PL signal, we can, in principle, analyze bulk lifetimes well below 0.1 μs. We find the analysis to be limited to about 0.1 μs in practice due to low SNR (0.1 suns, 30-s exposure). The calibration of a central high-lifetime grain with spectral PLIR can be verified with other techniques such as quasi-steady-state photoconductance (QSSPC) [19], dynamic PL [22], or full-spectrum PL measurements [56].

We performed the above analysis on the bottom section of the standard brick. Long-pass filtered images were captured, while central high lifetime regions were masked off using a black nonluminescent foil. The exposure time was extended to 30 s to ensure sufficient SNR. Note that this remains small in comparison with the dissociation time constant for bulk lifetimes below 3 μs and Fe–B concentration above 5×10^{12} cm^{-3}, which is calculated to be above 3 h for any typical combination of bulk lifetime and Fe–B concentration in this contaminated region. We obtained bulk lifetimes before and after Fe–B pair dissociation via the calibrated total PL transfer function and were then able to derive the interstitial iron concentration and the recombination fraction images [see Fig. 8(a)]. We find lifetimes in the range 0.4–3 μs in the paired state, and 0.1–1 μs in the dissociated state. The interstitial iron concentration was quantified to $2 - 4 \times 10^{13}$ cm^{-3} [see Fig. 8(b)] and assessed to be the dominant recombination path with almost 100% contribution to the total recombination [see Fig. 8(a)].

In practice, cropped bricks like the investigated standard-growth sample of this study often only have a narrow low-lifetime section without a real plateau area in the top (see, e.g., Fig. 4). This limited the analysis of the top in our sample due to residual light spreading caused by the signal gradient into the top section. In industrial production, bricks are available precropped with a larger top plateau that should allow the analysis of the top section as well with similar accuracy.

B. Iron Profiles, Uncertainties, and Comparison With Simulation

We determine the height profile of the interstitial iron concentration of the standard brick through a cross-sectional average alongside the large central grain structure averaging over a

2-cm-wide strip. Thus, we avoid any major influence of grain boundary artefacts on the profile. With reference to the above discussion, we believe that the spectral PLIR analysis is able to detect interstitial iron concentrations in areas with bulk lifetimes above 3 μs. For the standard brick studied in this paper, we are therefore able to measure interstitial iron concentrations in the range 1×10^{10} cm^{-3} to $\sim 4 \times 10^{12}$ cm^{-3} via the spectral PLIR analysis. This range represents the central $\sim 75\%$ of the standard-growth brick, which was cropped before the analysis by 4% at the bottom and 6% at the top. With respect to the total ingot height, the spectral PLIR analysis was thus able to quantify all but the bottom 15% and the top 8.5% of the standard-growth brick. However, that bottom section could be quantified with a PL intensity analysis as outlined above. The resulting measured interstitial iron profile of the standard-growth brick is depicted in Fig. 9. The narrow region between the total and the spectral analysis is not assessable directly but can be interpolated easily. The top section was not directly assessable on this sample as discussed above.

The total measurement accuracy of the lifetime-based method for measuring the dissolved iron concentration described in this study is mainly dependent on 1) the correctness of the electron capture cross section of interstitial iron in silicon $\sigma_n^{\mathrm{Fe}_i}$ and 2) the accuracy of the lifetime measurement itself. We estimate the uncertainty on the bulk lifetime within large grains to be within 20% [56], but it remains difficult to estimate the uncertainty of the capture cross sections, especially the electron capture cross section, which is the most relevant for low-injection measurements in p-type silicon [30], [40]. The uncertainty on the measured iron concentration of the bottom section is expected to be larger due to the lower SNR and residual light spreading artefacts from the transition region. Experimental verification of the measurement accuracy could, for example, be attempted via time-dependent analyses of the dissociation fraction of Fe–B pairs [26] but not through any other lifetime-based technique since they equally depend on the capture cross sections.

In the following, we aim to get more insight into the accuracy of our method through a comparison with modeling of the iron concentration in the crucible, lining, and ingot system. The contamination of the melted and solidified silicon by in-diffusion of iron from the crucible and coating is simulated with the approach and model parameters of [3]. We assume a uniform distribution of iron in the liquid silicon. The segregation process during solidification is calculated with a segregation coefficient of 2×10^{-5} at the liquid/solid interface [12]. The precipitation process during cool down, and thus, the Fe$_i$ concentration is simulated for a grain with a dislocation density of 5×10^3 cm^{-2}. The precipitation model [12], [57] used in this study successfully predicted the iron precipitate densities in mc-Si [10] and the interstitial iron concentrations after crystallization and solar cell processes [4], [7], [12].

The initial iron contamination of the feedstock, the crucible, and the lining were not known; hence, we chose approximate candidates for a brick that was grown in 2009 in a G4 crucible. The initial Fe contamination of the lining was chosen to be 30 ppm and for the crucible to be 100 ppm, referring to [5]. Based on a crystallization recipe for a small ingot [3], we
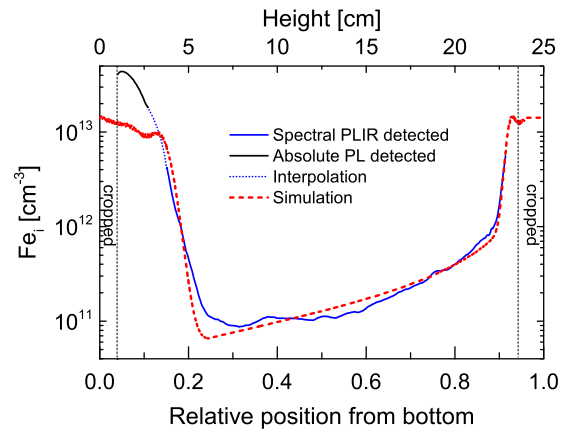

Fig. 9. Measured and simulated iron concentration of a standard-growth mc-Si brick as a function of brick height. The simulated data are compared with a cross-sectional average concentration along a central large grain structure. The central data are measured using deconvoluted full-field spectral PLIR, whereas the bottom section is analyzed through spectral PLIR calibrated PL intensities, the latter measured with partial masking of the brick during measurement. The top and bottom sections of the standard-growth brick were cropped prior to the measurement as indicated in the graph and, hence, could only be assessed experimentally in its remaining.

estimate the temperature distribution during the crystallization process of the G4 ingot: 27 h from melting until complete crystallization and 13 h of cool down. The first part of the process mainly influences the iron concentration in the central part and the total iron profile at the bottom, whereas the cooling rate below 1000 °C ($\sim$2.5 K/min) determines the fraction of interstitial iron. In areas with high total iron concentration (bottom, edge, and top), precipitation is quite effective after nucleation. At some temperature during cool down, the interstitial iron concentration is almost equal to the iron solubility and, thus, is independent of the total iron concentration. At lower temperatures, precipitation becomes limited by the diffusion of interstitial iron to the existing precipitates. The exact temperature at which most of the interstitial iron is not able to reach an existing precipitate, and thus, the height of the interstitial iron plateau is determined by the cooling rate.

The resulting simulated height profile using the above input parameters shows good correlation with the measured profile (see Fig. 9) over most parts of the brick. Only the bottom section is estimated to contain a lower concentration than measured and a more pronounced bottom plateau region is predicted in the simulation. The top transition region shows excellent agreement, while the experimental data in the bottom transition region decrease less steeply with ingot height than predicted by the model.

Lateral variations of the temperature result in lateral inhomogeneous diffusivities, which can lead to lateral inhomogeneous distributions of interstitial iron as found in (iii) Fig. 8(a). This can lead to a less steep transition [50], which additionally can be affected by different diffusivity and precipitation along grain boundaries that are present in the measured mc-Si sample but are not included in the simulation.

The measured interstitial iron concentration in the bottom section exceeds the simulated plateau concentration of $1 - 1.5 \times 10^{13}$ cm^{-3}. This is an indication that the dissociation of Fe–B pairs prior to the measurement of the dissociated bulk lifetime was complete or near complete ($>95\%$) in all parts of the brick face. An incomplete dissociation would lead to an underestimation of the interstitial iron concentration, which the comparison with the simulation does not suggest.

We reiterated the calculation of the dissociation fraction using (3) with the measured interstitial iron concentration shown in Fig. 4(a) after we initially calculated the Fe–B concentration, assuming it to be the only recombination center. We found minimal deviations in the resulting reiterated dissociation fraction. This is not surprising, since interstitial iron is in fact the dominant as-grown recombination path in the discussed standard-growth brick. Even though a reiteration can improve the analysis slightly, a dissociation analysis remains somewhat difficult for samples where other significant recombination channels are present, as discussed above.

The detection limit of this lifetime-based technique is strongly dependent on the density of defects other than interstitial iron and, hence, is a function of $\tau_{b,\text{other}}$. If we take the standard-growth Si brick of this study as an example, the detection limit is around 1×10^{10} cm^{-3} in the central part as the defect signal in the lifetime disappears for lower interstitial iron concentrations. However, in more highly defected bricks like the seeded-growth sample of this study, the detection limit is approximately 5×10^{10} cm^{-3}. Generally speaking, the more dominant the interstitial iron is in terms of the total recombination, the smaller the concentration that can be reliably detected.

The method demonstrated here should be applicable also to other p-doped bricks including compensated material, if the total acceptor concentration remains below about 5×10^{16} cm^{-3}, as the repairing may otherwise occur too rapidly. In addition, Cz-grown boron-doped silicon bricks or thick wafer/slabs can be measured in principle, but care needs to be taken with regard to possible interferences with the BO defect when dissociating Fe–B pairs [24].

VI. CONCLUSION

The spectral PLIR analysis can assess the spatially resolved bulk lifetime on the side faces of as-grown silicon bricks under true low-injection conditions with weighted average injection levels of below 1×10^{12} cm^{-3} and sufficient SNR. This is the ideal regime for accurate interstitial iron measurements as it 1) avoids the analysis of the injection dependence of the C-factor in (1); 2) minimizes the splitting of Fe–B pairs during the measurement of the paired state; 3) abolishes the need for accounting for the inhomogeneous injection carrier depth profile; and 4) relaxes the doping dependence of the C-factor.

We have found that 50 flashes from a 5500K equivalent Xenon flash lamp of 3200 J or above are sufficient to dissociate all Fe–B pairs within the scanned bulk, if Fe–B is a significant recombination path. This applies to all areas of the brick including the highly contaminated sections (bottom, top, and edge), although they are the most difficult to dissociate due to their shallow and low excess carrier profiles. A rigorous theoretical analysis of the dissociation fraction is currently limited to the case of dominating recombination through Fe–B pairs, since the dissociation rate constant for other cases is not known.

Highly resolved interstitial iron concentration images have been determined 1) using the standard spectral PL intensity ratio approach in central medium- to high-lifetime areas of the silicon bricks and 2) using a direct PL intensity analysis in the low-lifetime bottom section of one of the bricks. A direct PL intensity analysis extends the capabilities of PL-based analyses on bricks with bulk lifetimes down to 0.1 μs but is sensitive to doping variations and dependent on a calibration, which can be achieved through spectral PLIR or other methods.

Simulations of the iron distribution in the silicon ingot show good agreement with our measurement results. This result gives some additional confidence in the measurement accuracy regarding the concentration levels, the location of the transition regions, and the contamination levels in the highly contaminated bottom region.

Spectral PLIR images can provide bulk lifetime images with $\sim$20% uncertainty; hence, the total uncertainty of the dissolved iron concentration measurement is largely due to the uncertainty on the capture cross sections, especially the electron capture cross section of the Fe$_i$ defect. The uncertainty on the interstitial iron concentration is larger in the impure bottom and top sections due to low SNR and, if necessary, due to an additional doping correction.

The knowledge of both bulk lifetime and interstitial iron concentration represents an interesting spatially resolved set of material quality parameters at an early stage of solar cell production that has shown to be predictive of cell performance in the past [51]. We find interstitial iron to be the dominant recombination center in the as-grown state of the highly contaminated regions (bottom and top) of the two bricks discussed in this study with interstitial iron concentrations measured between 1×10^{13} and 5×10^{13} cm^{-3}.

ACKNOWLEDGMENT

REFERENCES

[1] J. Schmidt, B. Lim, D. Walter, K. Bothe, S. Gatz, T. Dullweber, and P. P. Altermatt, "Impurity-related limitations of next-generation industrial silicon solar cells," *IEEE J. Photovoltaics*, vol. 3, no. 1, pp. 114–118, Jan. 2013.

[2] D. Macdonald and L. J. Geerligs, "Recombination activity of interstitial iron and other transition metal point defects in p- and n-type crystalline silicon," *Appl. Phys. Lett.*, vol. 85, no. 18, pp. 4061–4063, 2004.

[3] M. C. Schubert, J. Schon, F. Schindler, W. Kwapil, A. Abdollahinia, B. Michl, S. Riepe, C. Schmid, M. Schumann, S. Meyer, and W. Warta, "Impact of impurities from crucible and coating on mc-silicon quality— The example of iron and cobalt," *IEEE J. Photovoltaics*, vol. 3, no. 4, pp. 1250–1258, Oct. 2013.

[4] F. Schindler, B. Michl, J. Schon, W. Kwapil, W. Warta, and M. C. Schubert, "Solar cell efficiency losses due to impurities from the crucible in multicrystalline silicon," *IEEE J. Photovoltaics*, vol. 4, no. 1, pp. 122–129, Jan. 2014.

[5] E. Olsen and E. J. Øvrelid, "Silicon nitride coating and crucible—Effects of using upgraded materials in the casting of multicrystalline silicon ingots," *Prog. Photovoltaics Res. Appl.*, vol. 16, no. 2, pp. 93–100, Mar. 2008.

[6] J. Tan, A. Cuevas, D. Macdonald, T. Trupke, R. Bardos, and K. Roth, "On the electronic improvement of multi-crystalline silicon via gettering and hydrogenation," *Prog. Photovoltaics Res. Appl.*, vol. 16, no. 2, pp. 129–134, Mar. 2008.

[7] B. Michl, J. Schön, W. Warta, and M. C. Schubert, "The impact of different diffusion temperature profiles on iron concentrations and carrier lifetimes in multicrystalline silicon wafers," *IEEE J. Photovoltaics*, vol. 3, no. 2, pp. 635–640, Apr. 2013.

[8] J. Hofstetter, J. F. Lelièvre, C. del Cañizo, and A. Luque, "Study of internal versus external gettering of iron during slow cooling processes for silicon solar cell fabrication," *Solid State Phenom.*, vol. 156–158, pp. 387–393, Oct. 2009.

[9] A. A. Istratov, H. Hieslmair, and E. R. Weber, "Iron and its complexes in silicon," *Appl. Phys. A Mater.*, vol. 69, pp. 13–44, 1999.

[10] J. Schön, A. Haarahiltunen, H. Savin, D. P. Fenning, T. Buonassisi, W. Warta, and M. C. Schubert, "Analyses of the evolution of iron-silicide precipitates in multicrystalline silicon during solar cell processing," *IEEE J. Photovoltaics*, vol. 3, no. 1, pp. 131–137, Jan. 2013.

[11] D. P. Fenning, J. Hofstetter, M. I. Bertoni, G. Coletti, B. Lai, C. del Cañizo, and T. Buonassisi, "Precipitated iron: A limit on gettering efficacy in multicrystalline silicon," *J. Appl. Phys.*, vol. 113, no. 4, pp. 044521-1–044521-12, 2013.

[12] J. Schön, H. Habenicht, M. C. Schubert, and W. Warta, "Understanding the distribution of iron in multicrystalline silicon after emitter formation: Theoretical model and experiments," *J. Appl. Phys.*, vol. 109, no. 6, pp. 063717-1–063717-8, 2011.

[13] J. Schön, H. Habenicht, M. C. Schubert, and W. Warta, "Simulation of iron distribution after crystallization of mc silicon," *Solid State Phenom.*, vols. 156–158, pp. 223–228, Oct. 2009.

[14] Y. Boulfrad, G. Stokkan, M. M'Hamdi, E. Øvrelid, and L. Arnberg, "Modeling of lifetime distribution in a multicrystalline silicon ingot," *Solid State Phenom.*, vol. 178–179, pp. 507–512, Aug. 2011.

[15] A. Liu, D. Walter, S. P. Phang, and D. Macdonald, "Investigating internal gettering of iron at grain boundaries in multicrystalline silicon via photoluminescence imaging," *IEEE J. Photovoltaics*, vol. 2, no. 4, pp. 479–484, Oct. 2012.

[16] A. Haarahiltunen, H. Savin, M. Yli-Koski, H. Talvitie, M. I. Asghar, and J. Sinkkonen, "As-grown iron precipitates and gettering in multicrystalline silicon," *Mater. Sci. Eng. B*, vol. 159–160, pp. 248–252, Mar. 2009.

[17] R. Kvande, L. J. Geerligs, G. Coletti, L. Arnberg, M. Di Sabatino, E. J. Ovrelid, and C. C. Swanson, "Distribution of iron in multicrystalline silicon ingots," *J. Appl. Phys.*, vol. 104, no. 6, pp. 064905-1–064905-9, 2008.

[18] D. Macdonald, A. Cuevas, A. Kinomura, Y. Nakano, and L. J. Geerligs, "Transition-metal profiles in a multicrystalline silicon ingot," *J. Appl. Phys.*, vol. 97, no. 3, pp. 033523-1–033523-7, 2005.

[19] J. S. Swirhun, R. A. Sinton, M. K. Forsyth, and T. Mankad, "Contactless measurement of minority carrier lifetime in silicon ingots and bricks," *Prog. Photovoltaics Res. Appl.*, vol. 19, no. 3, pp. 313–319, 2011.

[20] R. A. Sinton, T. Mankad, S. Bowden, and N. Enjalbert, "Evaluating silicon blocks and ingots with quasi-steady-state lifetime measurements," in *Proc.19th Eur. Photovoltaic Solar Energy Conf.*, 2004, pp. 520–523.

[21] N. Schüler, B. Berger, A. Blum, K. Dornich, and J. R. Niklas, "High resolution inline topography of iron in p-doped multicrystalline bricks by MDP," *Energy Procedia*, vol. 38, pp. 176–182, Jan. 2013.

[22] J. A. Giesecke, R. A. Sinton, M. C. Schubert, S. Riepe, and W. Warta, "Determination of bulk lifetime and surface recombination velocity of silicon ingots from dynamic photoluminescence," *IEEE J. Photovoltaics*, vol. 3, pp. 1–8, Oct. 2013.

[23] S. Herlufsen, K. Bothe, J. Schmidt, R. Brendel, and S. Siegmund, "Dynamic photoluminescence lifetime imaging of multicrystalline silicon bricks," *Sol. Energy Mater. Sol. Cells*, vol. 106, pp. 42–46, Nov. 2012.

[24] M. C. Schubert, H. Habenicht, and W. Warta, "Imaging of metastable defects in silicon," *IEEE J. Photovoltaics*, vol. 1, no. 2, pp. 168–173, Oct. 2011.

[25] A. Liu, Y. Fan, and D. Macdonald, "Interstitial iron concentrations across multicrystalline silicon wafers via photoluminescence imaging," *Prog. Photovoltaics Res. Appl.*, vol. 19, no. 6, pp. 649–657, 2011.

[26] S. Herlufsen, D. Macdonald, K. Bothe, and J. Schmidt, "Imaging of the interstitial iron concentration in crystalline silicon by measuring the dis-

[27] sociation rate of iron-boron pairs," *Phys. Status Solidi—Rapid Res. Lett.*, vol. 6, no. 1, pp. 1–3, Jan. 2012.

R. Hockett, "Advanced analytical techniques for solar-grade feedstock," *Adv. Silicon Mater. Photovoltaic Appl.*, pp. 215–234, 2012.

[28] M. Seibt and V. Kveder, "Gettering processes and the role of extended defects," *Adv. Silicon Mater. Photovoltaic Appl.*, pp. 127–188, 2012.

[29] T. Buonassisi, A. A. Istratov, M. A. Marcus, B. Lai, Z. Cai, S. M. Heald, and E. R. Weber, "Engineering metal-impurity nanodefects for low-cost solar cells," *Nat. Mater.*, vol. 4, no. 9, pp. 676–679, Sep. 2005.

[30] D. Macdonald, J. Tan, and T. Trupke, "Imaging interstitial iron concentrations in boron-doped crystalline silicon using photoluminescence," *J. Appl. Phys.*, vol. 103, no. 7, pp. 073710-1–073710-7, 2008.

[31] B. Mitchell, T. Trupke, J. W. Weber, and J. Nyhus, "Bulk minority carrier lifetimes and doping of silicon bricks from photoluminescence intensity ratios," *J. Appl. Phys.*, vol. 109, no. 8, pp. 083111-1–083111-12, 2011.

[32] B. Mitchell, J. W. Weber, D. Walter, D. Macdonald, and T. Trupke, "On the method of photoluminescence spectral intensity ratio imaging of silicon bricks: Advances and limitations," *J. Appl. Phys.*, vol. 112, no. 6, pp. 063116-1–063116-13, 2012.

[33] SEMI, (2013). International Technology Roadmap for Photovoltaic (ITRPV) Results 2012. [Online]. Available: www.pvgroup.org

[34] B. Mitchell, J. W. Weber, M. Juhl, D. Macdonald, and T. Trupke, "Photoluminescence imaging of silicon bricks," *Solid State Phenom.*, vol. 205–206, pp. 118–127, 2013.

[35] G. Zoth and W. Bergholz, "A fast, preparation-free method to detect iron in silicon," *J. Appl. Phys.*, vol. 67, no. 11, pp. 6764–6771, 1990.

[36] L. J. Geerligs and D. Macdonald, "Dynamics of light-induced FeB pair dissociation in crystalline silicon," *Appl. Phys. Lett.*, vol. 85, no. 22, pp. 5227–5229, 2004.

[37] D. H. Macdonald, L. J. Geerligs, and A. Azzizi, "Iron detection in crystalline silicon by carrier lifetime measurements for arbitrary injection and doping," *J. Appl. Phys.*, vol. 95, no. 3, pp. 1021–1028, 2004.

[38] D. K. Schroder, "Surface voltage and surface photovoltage: History, theory and applications," *Meas. Sci. Technol.*, vol. 12, no. 3, pp. R16–R31, Mar. 2001.

[39] M. C. Schubert, M. J. Kerler, and W. Warta, "Influence of heterogeneous profiles in carrier density measurements with respect to iron concentration measurements in silicon," *J. Appl. Phys.*, vol. 105, no. 11, pp. 114903-1–114903-6, 2009.

[40] D. Macdonald, T. Roth, P. N. K. Deenapanray, T. Trupke, and R. A. Bardos, "Doping dependence of the carrier lifetime crossover point upon dissociation of iron-boron pairs in crystalline silicon," *Appl. Phys. Lett.*, vol. 89, no. 14, pp. 142107-1–142107-3, 2006.

[41] J. Tan, D. Macdonald, F. Rougieux, and A. Cuevas, "Accurate measurement of the formation rate of iron-boron pairs in silicon," *Semicond. Sci. Technol.*, vol. 26, no. 5, pp. 055019-1–055019-7, May 2011.

[42] S. Y. Lim and D. Macdonald, "Measuring dopant concentrations in p-type silicon using iron-acceptor pairing monitored by band-to-band photoluminescence," *Sol. Energy Mater. Sol. Cells*, vol. 95, no. 8, pp. 2485–2489, Aug. 2011.

[43] F. Recart, H. Mackel, A. Cuevas, and R. A. Sinton, "Simple data acquisition of the current-voltage and illumination-voltage curves of solar cells1," in *Proc. 4th IEEE World Conf. Photovoltaic Energy Convers.*, 2006, pp. 1215–1218.

[44] P. A. Basore and D. A. Clugston, "PC1D," in *Proc. 25th IEEE Photovoltaic Spec. Conf.*, 1996, pp. 377–383.

[45] B. Mitchell, J. Greulich, and T. Trupke, "Quantifying the effect of minority carrier diffusion and free carrier absorption on photoluminescence bulk lifetime imaging of silicon bricks," *Sol. Energy Mater. Sol. Cells*, vol. 107, pp. 75–80, 2012.

[46] K. Bothe, R. Sinton, and J. Schmidt, "Fundamental boron-oxygen-related carrier lifetime limit in mono- and multicrystalline silicon," *Prog. Photovoltaics Res. Appl.*, vol. 13, no. 4, pp. 287–296, Jun. 2005.

[47] D. Macdonald, A. Cuevas, and L. J. Geerligs, "Measuring dopant concentrations in compensated p-type crystalline silicon via iron-acceptor pairing," *Appl. Phys. Lett.*, vol. 92, no. 20, pp. 202119-1–202119-3, 2008.

[48] S. Bowden and R. A. Sinton, "Determining lifetime in silicon blocks and wafers with accurate expressions for carrier density," *J. Appl. Phys.*, vol. 102, no. 12, pp. 124501-1–124501-7, 2007.

[49] D. Walter, A. Fell, E. Franklin, D. Macdonald, B. Mitchell, and T. Trupke, "The impact of silicon CCD photon spread on quantitative analyses of luminescence images," *IEEE J. Photovoltaics*, vol. 4, no. 1, pp. 368–373, Jan. 2014.

[50] Y. Boulfrad, A. Haarahiltunen, H. Savin, E. J. Øvrelid, and L. Arnberg, "Enhanced performance in the deteriorated area of multicrystalline silicon

wafers by internal gettering," *Prog. Photovoltaics Res. Appl.*, in press, Jul. 2013.

[51] L. J. Geerligs, "Impact of defect distribution and impurities on multicrystalline silicon cell efficiency," in *Proc. 3rd World Conf. Photovoltaic Energy Convers.*, 2003, pp. 1044–1047.

[52] S. P. Phang and D. Macdonald, "Direct comparison of boron, phosphorus, and aluminum gettering of iron in crystalline silicon," *J. Appl. Phys.*, vol. 109, no. 7, pp. 073521-1–073521-6, 2011.

[53] J. Hofstetter, D. P. Fenning, M. I. Bertoni, J. F. Lelièvre, C. del Cañizo, and T. Buonassisi, "Impurity-to-efficiency simulator: Predictive simulation of silicon solar cell performance based on iron content and distribution," *Prog. Photovoltaics Res. Appl.*, vol. 19, no. 4, pp. 487–497, 2011.

[54] M. D. Pickett and T. Buonassisi, "Iron point defect reduction in multicrystalline silicon solar cells," *Appl. Phys. Lett.*, vol. 92, no. 12, pp. 122103–122103-3, 2008.

[55] E. Scheil, "Bemerkungen zur Schichtkristallbildung," *Zeitschrift fuer Met.*, vol. 34, no. 3, pp. 70–72, 1942.

[56] B. Mitchell, M. K. Juhl, M. A. Green, and T. Trupke, "Full spectrum photoluminescence lifetime analyses on silicon bricks," *IEEE J. Photovoltaics*, vol. 3, no. 3, pp. 962–969, Jul. 2013.

[57] A. Haarahiltunen, H. Väinölä, O. Anttila, M. Yli-Koski, and J. Sinkkonen, "Experimental and theoretical study of heterogeneous iron precipitation in silicon," *J. Appl. Phys.*, vol. 101, no. 4, pp. 043507-1–043507-6, 2007.

Authors' photographs and biographies not available at the time of publication.